Available online at www.sciencedirect.com
ScienceDirect
International Journal of Thermal Sciences 48 (2009) 805–814
International Journal of Thermal Sciences
www.elsevier.com/locate/ijts

Numerical study on the thermal characteristics in a tubular solid oxide fuel cell with indirect internal reformer

Xiongwen Zhang, Jun Li, Guojun Li *, Zhenping Feng

School of Energy & Power Engineering, Xi'an Jiaotong University, China

Received 26 July 2007; received in revised form 25 May 2008; accepted 26 May 2008

Available online 26 June 2008

Abstract

Numerical simulation was implemented on a tubular solid oxide fuel cell (SOFC) with indirect internal reformer used in the demonstration projects of Siemens–Westinghouse. The Navier–Stokes equations and the charge equation were solved by means of a generalized, three-dimensional complete polarization electrochemical model for SOFC. The distributions of both the molar fraction of gaseous species and the temperature were presented. The characteristic of thermal energy generation was analyzed based on the simulation results. The electrochemical process was exothermic reaction, which contributed 82.7% in the total heat generation. The ohmic heat possessed 17.3% in the total heat generation. About 47.3% of the generated heat in the cell was absorbed by the reforming reaction. The air flow took away 36.6% the generated heat and the remainder 16% was taken away by the fuel flow.

Keywords: Tubular solid oxide fuel cell; Numerical simulation; Thermal characteristics

1. Introduction

Solid oxide fuel cells (SOFCs) are power generation devices that convert the chemical energy directly to electrical energy by electrochemical reaction. It is considered as one of the most important technologies to solve the energy and environmental problems in the future thanks to its high efficiency and low emission. As a high temperature fuel cell, the SOFC can be combined with a gas turbine (GT) to form hybrid cycle. The electric efficiency of hybrid cycles of SOFC/GT is believed to reach more than 75% (LHV) while fueled with natural gas [1]. Moreover, SOFC can be made in various geometries such as planar, tubular, and monolith attributed to the solid electrolyte being used in SOFCs. The commercial SOFC is expected to have lifetime of 10 to 20 years, two to four times longer than other type fuel cells [2]. For these good advantages, SOFC research has been accelerated since 2000. In particular, some demonstrations have been performed by Siemens–Westinghouse based on the tubular SOFC [3].

Thermal characteristic has an important impact on the performance of SOFC. The solid thermal stress and the stack cooling are closely correlated with the thermal characteristic in the design of SOFC. Furthermore, the temperature has strong effect on the chemical reactions and on the conductivity property of electric material, which affect the electric characteristics of fuel cell and the distribution of gaseous molar fraction. In current, detailed information in the fuel cell was acquired mostly by numerical method due to the complex geometry, the high operating temperature, and complicated physical processes in the fuel cell. Although many previous publications [4–11] calculated the parameters distribution (e.g. gas species, current density, voltage, temperature and polarization losses) using numerical method, thermal characteristic on view of macrograph as an important factor in the design of SOFC was scarcely reported. For example, as coolant medium of fuel cell stack, both the air flow and the fuel reforming process absorb the generated thermal energy in fuel cell. In order to design the stoichiometric times of air flow and the fuel internal reforming ratio under a definite operating load of SOFC, we need to calculate the proportion of the absorbed thermal energy by air flow and by the fuel internal reforming, respectively. We studied the electric characteristics and the generated ohmic heat on a single

* Corresponding author.
E-mail address: liguojun@mail.xjtu.edu.cn (G. Li).

1290-0729/$ – see front matter
doi:10.1016/j.ijthermalsci.2008.05.016

Nomenclature

a	absorption coefficient
a_s	scattering coefficient
A_{CV}	the specific surface area of control volume .. m^{-1}
c_p	specific heat capacity ..... $\mathrm{J\,mol^{-1}\,K}$
D	diffusion coefficient ..... $\mathrm{m^{-2}\,s^{-1}}$
div	operation symbol – calculate divergence
E	activation energy ..... $\mathrm{J\,mol^{-1}}$
E_n	Nernst potential V
E_v	voltage V
F	Faraday constant ..... $= 96485\ \mathrm{C\,mol^{-1}}$
f_e	equilibrium factor for reforming reaction
g	molar Gibbs free energy ..... $\mathrm{J\,mol^{-1}}$
G	Gibbs free energy ..... J
grad	operation symbol – calculate gradient
h	molar enthalpy ..... $\mathrm{J\,mol^{-1}}$
ΔH	change of enthalpy for chemical reaction $\mathrm{J\,mol^{-1}}$
I	radiation intensity
i	current density ..... $\mathrm{A\,m^{-2}}$
i_0	exchange current density ..... $\mathrm{A\,m^{-2}}$
K	equilibrium constant
k	stoichiometric reaction coefficient
k_0	constant parameter for the rate of reforming reaction ..... $\mathrm{mol\,s^{-1}\,m^{-2}}\ p_a^{-1}$
k_1	constant parameter for the rate of shift reaction ..... $\mathrm{mol\,m^{-3}\,s^{-1}}$
M	molecular mass
n	refractive index
$\vec{n}$	the unit normal vector
n_e	electrons transferred per reaction
p	pressure ..... Pa
p^{e}	evaluation value of pressure ..... Pa
P_0	standard pressure ..... Pa
q	heat transfer rate ..... $\mathrm{J\,s^{-1}}$
Q	heat source ..... $\mathrm{W\,m^{-3}}$
$\dot{r}$	volumetric reaction rate ..... $\mathrm{mol\,s^{-1}\,m^{-3}}$
$\vec{r}$	position vector
R	universal gas constant ..... $= 8.314\ \mathrm{J\,mol^{-1}\,K^{-1}}$
R_n	area specific resistance ..... $\Omega\,\mathrm{m^{-2}}$
S	source component
s	molar entropy ..... $\mathrm{J\,mol^{-1}\,K^{-1}}$
$\vec{s}$	direction vector
$\vec{s}'$	scattering direction vector
T	temperature ..... K
V	velocity ..... $\mathrm{m\,s^{-1}}$
Y	mass fraction of gas species
w	rate of work ..... $\mathrm{J\,s^{-1}}$

Greek letters

α	the permeability of porous material
β	current transfer coefficient
β_1, β_2	coefficients of Eq. (8)
η	polarization V
δ_{el}	thickness of electrolyte ..... m
ρ	fluid density ..... $\mathrm{kg\,m^{-3}}$
σ	conductivity ..... $\mathrm{S\,m^{-1}}$
σ_s	Stefan–Boltzmann constant ..... $5.672 \times 10^{-8}\ \mathrm{W\,m^{-2}\,K^{-4}}$
Φ	electric potential V
ζ	inertial resistance factor
λ	heat conductivity ..... $\mathrm{W\,m^{-1}\,K^{-1}}$
γ	coefficient in Eqs. (4), (5)
μ	fluid viscosity ..... Pa s
Γ	diffusion coefficient of control equations
Θ	phase function
Ω	solid angle
Σ	surface of control volume

Subscript

a	anode
b	back
act	activation
c	cathode
chem	chemical reaction
conc	concentration
E	electrochemical oxidize reaction
el	electrolyte
f	forward
i	chemical species
j	direction of coordinate
ohm	ohmic
rad	radiant
ref	reference
R	reforming reaction
S	shift reaction
tot	total

planar SOFC with various gas flow configuration and a single tubular SOFC fueled with hydrogen in reference [12]. However, in real operation of a tubular SOFC stack, neighbor cells affect each other. Furthermore, the fuel reformer is often indirectly internally reformer and thermally integrated with the tube bundle. The fuel reforming process has strong influence on the parameters distribution in the cell. Therefore, it is valuable to investigate the thermal characteristics in the tubular SOFC stack with internal reformer. In this study, a tubular SOFC stack with indirect internal reformer configuration is investigated.

A complete generalized polarization mathematical model of SOFC was presented by Chan [13]. According to this mathematical model, a three-dimensional numerical model is developed in this study. The electrochemical model equations are solved coupled with Navier–Stokes equations and charge equation. Numerical simulation is implemented on the tubular SOFC stack issued by Siemens–Westinghouse with the help of the computational fluid dynamic (CFD) software Fluent 6.1. The distribution for both of the gaseous species molar fraction and the temperature are presented according to the simulation re-

sults. The electrochemical generated heat, the ohmic generated heat, the air flow absorbed heat, the fuel flow absorbed heat, and the reformer absorbed heat are calculated and analyzed in detail.

2. SOFC model

2.1. Description of a tubular SOFC configuration

The most common original design of tubular SOFC was issued by Westinghouse Electric Corporation (now Siemens–Westinghouse Power Corporation), which the cell components are deposited in the form of thin layers on a cylindrical tube. Since 1986, Siemens–Westinghouse has tested several fully integrated SOFC systems on customer sites, ranging from 0.4 kW to 220 kW [3,14]. One of the most recent demonstrations was a 100 kW atmospheric SOFC-CHP system sponsored initially by EDB/ELSAM, a consortium of Dutch and Danish utilities. Fig. 1 shows the scheme of the tubular SOFC field unit modular for the 100 kW demonstration. The SOFC field unit was fuelled with natural gas and was operated as an auxiliary district heat plant near Arnhem in Netherlands between 1998 and 2000. This system supply AC power to the utility grid and hot water to the district heating system serving the Duiven/Westervoort area. It generates approximately 110 kW net AC power at 46% efficiency (LHV) and nearly 75% energy efficiency [3]. This SOFC-CHP unit was moved to Essen, Germany in July 2001 and Torino, Italy in July 2004 [15,16]. Fig. 1(a) shows the external geometry of the sub-stack that consists of 576 unit-cell. That is also the basic unit building block used in the others Siemens–Westinghouse demonstrations. Each of the sub-stacks has its own ejector and pre-reformer. A gas plenum is deployed as air distribution at the uppermost of sub-stack. In the stack (see Fig. 1(b)), four cell bundles are connected in series to form a bundle row, and 12 bundle rows are aligned side by side, interconnected in serpentine fashion with an in-stack reformer between each bundle row. This stack can be viewed as composed of two basic unit sub-stacks. The next level of fabrication hierarchy after the cell is the cell bundle. As Fig. 1(c) shows, the cell bundle is central symmetric configuration, consisting of a 24-cell array arranged as eight cells in electrical series by three cells in electrical parallel. The dimensions of the unit cell are 22 mm diameter, 1500 mm active length with 834-cm^2 active area.

Fig. 2 shows the details gases flow route in the stack. The stack is separated horizontally into five zones by ceramic baffles in the vertical. These five zones are as follows: the fuel distribution plenum below the cell stack, the active cell space, the depleted fuel plenum, the combustion zone above the cell stack, and the air plenum. Desulfurized natural gas is introduced as the primary fluid in an ejector. The incoming natural gas mixes with the recirculated exhaust stream, which is from the depleted fuel plenum in the anode. A small percentage of methane is reformed in the adiabatic pre-reformer. The mixture is then routed to the top of the in-stack reformers from where it flows downward through a catalytically active space to the fuel distribution plenum. The in-stack reformers are heated radiantly

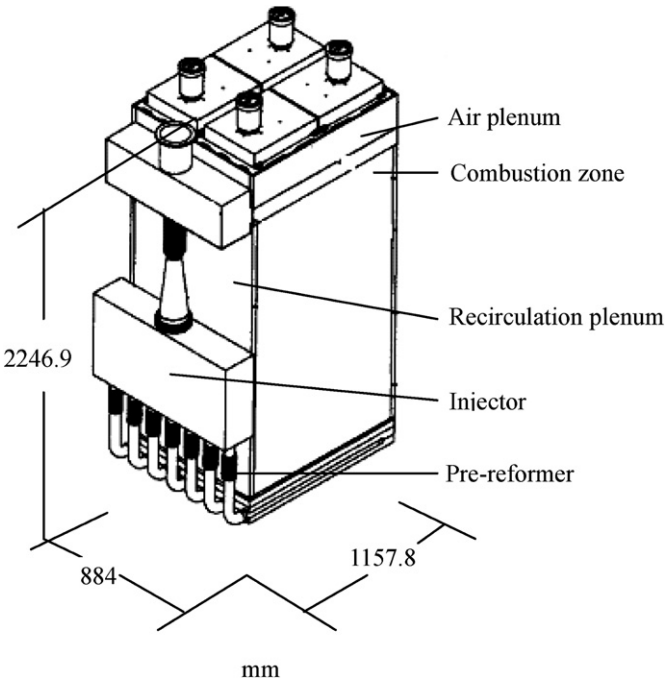

(a) The basic unit building block (576 cell substack) [3]

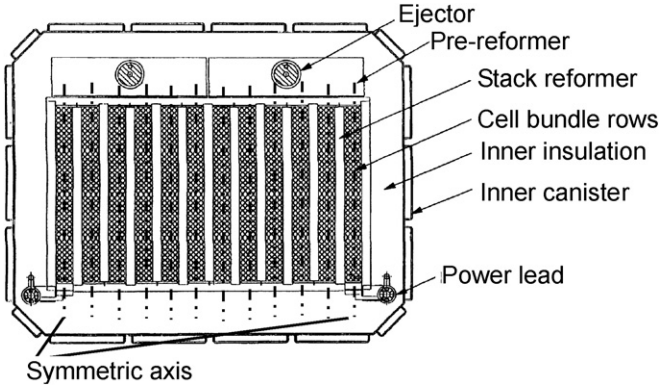

(b) The cross-section of stack [17]

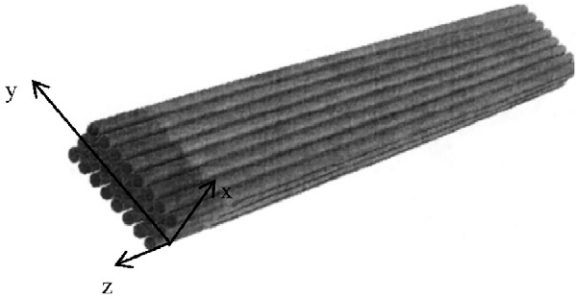

(c) The typical 24-cell bundle of tubular SOFCs [17]

Fig. 1. The typical tubular SOFC designed by Siemens–Westinghouse Corporation [3,17].

by the fuel cells. The fully reformed fuel passes over the exterior of the fuel cell where it is electrochemically reacted. The depleted fuel is passed to the fuel plenum where some of the exhaust fuel is recirculated and the other passes to the combustion zone. Air is introduced into the air plenum and is routed to the interior and the bottom of each tubular cell by an air feed

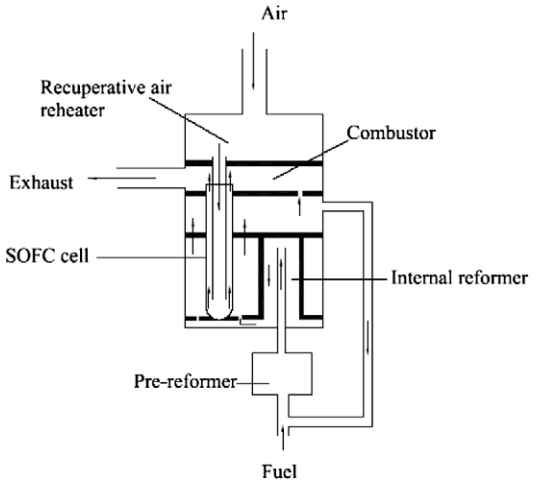

Fig. 2. The internal configuration of the Siemens–Westinghouse tubular SOFC [17].

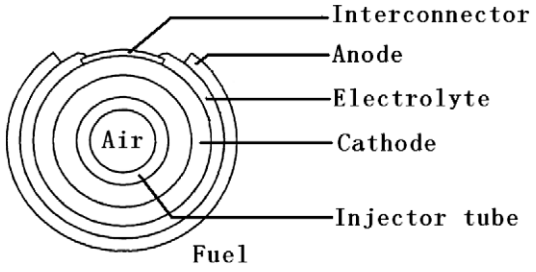

Fig. 3. Cross-section of unit-cell of tubular SOFC [1,4].

tube. The air passes upward in the annular space between the cell cathode and the air feed.

As shown in Fig. 2, methane is reformed in the in-stack reformer board, which is separated from the tubular anode space by a baffle-wall. The required energy for reforming reaction is provided by the heat exchange between the fuel cells active zones and the reformer zones. This indirect internal reforming (IIR) configuration is different from the direct internal reforming (DIR) configuration, where the methane is directly reformed on the anode.

The schematic cross-section of the tubular SOFC with Siemens–Westinghouse design is shown in Fig. 3. In this SOFC, the thickness of the electrolyte and the outer anode layer are 40 μm and 100 μm, respectively. Since it is a cathode supported cell, the cathode thickness is designed as 2200 μm, which is larger than those of electrolyte and anode. The electrode porosity is 30–40%. At the bottom of the cell there is the current collection component named inter-connector. Its thickness is 80 μm. The cathode is continuously throughout the cylinder. The electrolyte acts through 312° of the circumference and it is interrupted by the inter-connector. The anode is also discontinuous, acting through a circumference of 288°, leaving the opening for electrical contact to the adjacent cell [1–3].

2.2. Electrochemical models

From the pre-reformer outlet, the fuel mixture first flows into the in-stack reformer. The residual methane is reformed in the catalyze layer. The reforming reaction equation is written as follows:

$$CH_4 + H_2O \rightarrow CO + 3H_2$$

The reversible gas-shift reaction is included in both the in-stack reformer and the anode.

$$CO + H_2O = CO_2 + H_2$$

More than 99% methane is converted into hydrogen after the in-stack reformer.

The electrochemical reactions occur at the interfaces between electrolyte and electrode. H_2 is oxidized at the anode and the released electrons are transported to the cathode through the external electric circuit. Combing with the electrons, O_2 is reduced to the oxygen anions at the cathode. The oxygen anions are transported through the electrolyte to the anode and react with H_2. The overall reaction is expressed as follows:

$$1/2O_2 + H_2 \rightarrow H_2O$$

Additionally, the carbon monoxide is oxidized at the anode:

$$CO + O^{2-} \rightarrow CO_2 + 2e^-$$

However, the reaction velocity of CO oxidation is 2–5 times [8] slower than that of hydrogen oxidation. The rapid gas-shift reaction becomes the dominant reaction. Therefore, the oxidation of carbon monoxide is neglected in this study.

The voltage of electrochemical reaction is modeled as follows:

$$E_v = -\frac{1}{n_e F}\left[\sum_i (k_i g_i)_p - \sum_i (k_i g_i)_r\right] - \eta_{\text{act}} - \eta_{\text{ohm}} - \eta_{\text{con}} \quad (1)$$

where

$$g_i(T, p_i) = h_i(T) - T s_i(T, p_i) = \int_{T_0}^{T} c_{pi}(T)\,dT - T\int_{T_0}^{T} \frac{c_{pi}(T)}{T}\,dT - RT\ln\frac{P_0}{p_i^{\text{e}}} \quad (2)$$

The voltage loss for polarizations, which include the activation polarization, the ohmic polarization, and the concentration polarization, are calculated at the anode and the cathode respectively. Very often, the activation polarization calculation was simplified with Tafel equation and the Knudsen diffusion was neglected in the gas diffusion through the porous electrodes. To avoid the ambiguity of the suitability of such models used in the calculation of cell polarization. This work employ a complete polarization model [13], which uses the Butler–Volmer equation to calculate activation polarization and considers the Knudsen diffusion in the modeling of concentration polarization.

For both the anode and the cathode sides, the activation polarization is calculated by Butler–Volmer equation:

$$\eta_{\text{act}} = \frac{2RT}{n_e F}\sinh^{-1}\left(\frac{i}{2i_0}\right) \quad (3)$$

The current exchange i_0 is the function of the local species concentration and temperature. The model is formulized as follows:

At the anode

$$i_0 = \gamma_a \left(\frac{p_{H_2}}{p_{ref}}\right)\left(\frac{p_{H_2O}}{p_{ref}}\right)\exp\left(-\frac{E_a}{RT}\right) \tag{4}$$

At the cathode

$$i_0 = \gamma_c \left(\frac{p_{O_2}}{p_{ref}}\right)^{0.25}\exp\left(-\frac{E_c}{RT}\right) \tag{5}$$

The partial pressures of reactive species, which are employed to calculate the Nernst potential in Eq. (1) are not the local values at the reaction site. In the present model, these parameters are determined by the corresponding local values at the control volume grid cell adjacent to the reaction surface. Therefore, correction to the actual gas partial pressures both at the anode and at the cathode is necessary. The correction is generally called concentration polarization. The concentration polarizations are modeled as follows [13]:

At the anode

$$\begin{aligned}\eta_{conc,a} &= -\frac{RT}{2F}\left[\ln\left(\frac{p_{H_2}}{p^e_{H_2}}\right) - \ln\left(\frac{p_{H_2O}}{p^e_{H_2O}}\right)\right] \\ &= -\frac{RT}{2F}\ln\left[\frac{1-(RTl_a|\vec{i}\cdot\vec{n}|)/(2FD_{a(eff)}p^e_{H_2})}{1+(RTl_a|\vec{i}\cdot\vec{n}|)/(2FD_{a(eff)}p^e_{H_2O})}\right]\end{aligned} \tag{6}$$

At the cathode

$$\begin{aligned}\eta_{conc,c} &= -\frac{RT}{4F}\ln\left(\frac{p_{O_2}}{p^e_{O_2}}\right) \\ &= -\frac{RT}{4F}\ln\left\{\left((p_c/\delta_{O_2}) - \left[(p_c/\delta_{O_2}) - p^e_{O_2}\right]\right.\right. \\ &\quad \left.\left.\times\exp\left[\left(RT\delta_{O_2}l_c|\vec{i}\cdot\vec{n}|\right)/(4FD_{O_2(eff)}p_c)\right]\right)/p^e_{O_2}\right\}\end{aligned} \tag{7}$$

where $\vec{n}$ is the normal vector and l is the distance calculated from the center of the neighbor grid cell to the electrolyte interface, and

$$\delta_{O_2} = \frac{D_{O_2,K(eff)}}{D_{O_2,K(eff)} + D_{O_2-N_2(eff)}}$$

The conductivity of these components is the function of the temperature. It is modeled by the following equations:

$$\sigma = \beta_1 \exp\left(-\frac{\beta_2}{T}\right) \tag{8}$$

For the electrolyte, the ohmic polarization is described as

$$\eta_{ohm} = \delta_{el} i/\sigma \tag{9}$$

The methane reforming rate has been modeled by many researchers. In the present study, following equation is employed [8,18]

$$\dot{r}_R = k_0 p_{CH_4} f_e \exp\left(\frac{-\Delta E}{RT}\right) \tag{10}$$

where the equilibrium factor f_e is approximated as 1. The reaction rates of the shift reaction are determined by the forward and the backward processes [19]

$$\dot{r}_f = k_1 p_{CO} p_{H_2O} \tag{11a}$$

$$\dot{r}_b = k_1 K_{shift} p_{CO_2} p_{H_2} \tag{11b}$$

where k_1 is a constant and equals to 1.2×10^4 mol/m^3 s. The equilibrium constant is expressed as

$$K_{shift} = \exp\left(\frac{-\Delta G_{wgs}}{RT}\right) \tag{12}$$

and the change of Gibbs free energy is calculated by Eq. (2).

3. Numerical method

The governing equations such as the continuity conservation, momentum conservation, energy conservation, species transport, and electric potential equation are solved at the control volume. The generalized form of the steady governing equations is written as follows [20]:

$$\mathrm{div}(\rho\vec{V}\phi) = \mathrm{div}(\Gamma_\phi \,\mathrm{grad}\,\phi) + S_\phi \tag{13}$$

where ϕ is a generalized variable. For the continuity equation, $\phi = 1$. For other control equations, ϕ is replaced by the mass fraction of each species Y_i for the transport equations, the velocity V_j for momentum equations, the temperature T for energy equation, and the electric potential Φ for the charge equation. Γ_ϕ is the diffusion coefficient and S_ϕ is the source term for the general variable ϕ. To the species transport equations, dilute approximation is applied in the laminar flow. For the electric potential equation, the diffusion coefficient Γ_Φ equals to the material electric conductivity.

Laminar model and SIMPLEC algorithm are employed in the simulation. The species transport equations are solved for seven species: H_2, O_2, H_2O, CH_4, CO, CO_2, and N_2. The fluid convection is assumed to have no effect on the electric conductivity. Then, the convection term of the electric potential equation could be set to zero within the fluid zones.

The heat source of energy equation is the sum of the ohmic heat term, the chemical reaction heat term and the radiant heat exchange. In present model, we neglects absorption, emission or scattering in the gas media and only accounts for the surface-to-surface radiation effects in the simulation. The discrete ordinates (DO) radiation model is applied to calculate the radiant heat exchange [21]. The field radiative transfer equation is written as

$$\begin{aligned}&\nabla\cdot\left(I(\vec{r},\vec{s})\vec{s}\right) + (a+a_s)I(\vec{r},\vec{s}) \\ &\quad = an^2\frac{\sigma_s T^4}{\pi} + \frac{a_s}{4\pi}\int_0^{4\pi} I(\vec{r},\vec{s})\Theta(\vec{s}\cdot\vec{s}')\,d\Omega\end{aligned} \tag{14}$$

In the simulation, the radiative transfer equation is solved for a finite number of discrete solid angles, each associated with a vector direction, $\vec{s}$, fixed in the global Cartesian system. The radiant heat exchange is calculated by integrating the radiative transfer equation over the surface of control volume:

$$Q_{rad} = \int_\Sigma I\cdot\vec{s}\cdot\vec{n}\,d\Sigma \tag{15}$$

In the electric zone, the ohmic heat source was given by

$$Q_{ohm} = \sigma \,\mathrm{grad}\,\Phi\,\mathrm{grad}\,\Phi \tag{16}$$

The chemical heat source in the anode is expressed as follows:

$$Q_{\text{chem}} = (\dot{r}_{\text{f}} - \dot{r}_{\text{b}})\Delta H_S + \dot{r}_R \Delta H_R + \Delta H_E A_{CV} |\vec{i} \cdot \vec{n}|/(2F) \quad (17)$$

Therefore, the following equation is obtained:

$$S_q = Q_{\text{ohm}} + Q_{\text{chem}} + Q_{\text{rad}} \quad (18)$$

The mass source term of species is calculated according to the rate of chemical reaction, abides by the following equation

$$S_i = M_i \left[k_{R,i} \dot{r}_R + \kappa_{s,i} (\dot{r}_{\text{f}} - \dot{r}_{\text{b}}) + \kappa_{e,i} |\vec{i} \cdot \vec{n}|/(2F) \right] \quad (19)$$

In addition, porous media is modeled by adding a momentum source term to the standard fluid flow equations. The source term consists of a viscous loss term and an inertial loss term, which is given as follows [21]:

$$S_j = -\left(\sum_{k=1}^{3} D_{j,k} \mu V_k + \sum_{k=1}^{3} \zeta_{j,k} \frac{1}{2} \rho |\vec{V}| V_k \right) \quad (20)$$

where j denotes the jth (x, y, or z) momentum equation, and D and ζ are prescribed matrices. In the present simulation, the porous medium is simply considered as homogeneous. For the laminar model, the pressure drop is typically proportional to velocity and the constant ζ could be considered to be zero. Then the porous media model can be described by Darcy's Law [21]:

$$S_j = -\frac{\mu}{\alpha} V_j \quad (21)$$

At the interface between the electrolyte and the electrode, the current density through the electrolyte is obtained according to the following equation

$$i = \frac{E_n - (\Phi_{\text{c}} - \Phi_{\text{a}})}{R_n} \quad (22)$$

where R_n is local lumped electric resistance including ohmic resistance of the electrolyte and polarization losses of electrodes. At the external boundary, the thermal flux and the electric current flux are zero. A uniform potential is assumed and its value is given at the current inlet and outlet. The temperature, the species mass fractions and the mass fluxes are imposed at the gas inlet. The pressure is given at the gas outlets.

4. Numerical simulation results

Fig. 4 shows the topology of computational domain in present simulation. Since each bundle of cell with a row internal stack reformer has an axisymmetric geometry, the symmetric boundary condition and the periodic boundary condition could be employed in the simulation. Only one and half neighbor cell with half of internal reformer is simulated in present study. But in order to simplify the computational geometry, we assume that the temperature is uniform over the cross section of the fuel feed tube in the internal reformer. The computational domain excludes the fuel feed tube and the fuel inlet is moved to the top of fuel feed tube (see Fig. 4). The fuel inlet is adjacent to the exhaust gas where the temperature is around 1073 K [1]. This work specifies the fuel inlet temperature 1023 K giving −50 K grads to the exhaust gas temperature. Both of the heat

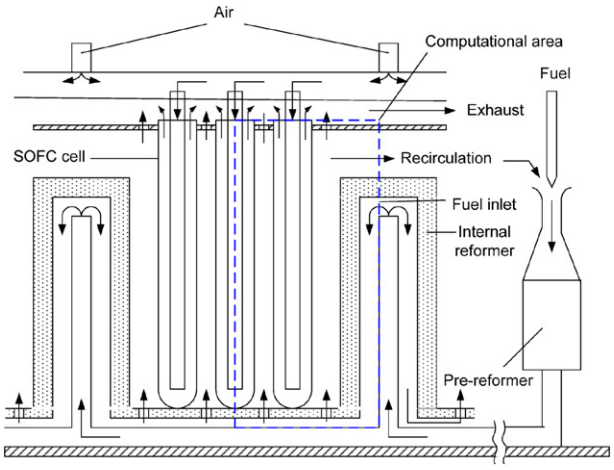

Fig. 4. The topology of the computational domain and gases flow configuration.

flux and the electric current flux at the external wall boundary are assumed as zero. The temperature and the mass fractions of species as well as the mass fluxes are imposed at the gas inlet, while the pressure is given at the gas outlets. The operating conditions are specified in Table 1.

The computational domain is composed of the anode, the cathode, the inter-connector, the contact, the reformer catalyzed zone, and the gas flow channels. The electrolyte is considered as solid wall and the inter-connector is solid zone. The porous zones include the anode, the cathode, the contact and the reformer catalyzed zone. Both of the construct and the non-construct topology grids are applied to each of these zones according to the geometry. The total grid cell is about 711 160 for the whole computational domain. The interior interface condition is employed between the fuel flow and the anode zone, the air flow and the cathode zone, and the fuel flow and the catalyzed zone within the reformer. Compared to the fuel cell dimension, the anode thickness 100 μm is too thin to generate a good topology grid that has impact on the simulation convergence and numerical accuracy. Therefore, in this study, the anode thickness is expanded to 1000 μm and its electric conductivity is reduced correspondingly 10 times. The detailed information of the grid topology around the electrolyte is illustrated in Fig. 5.

Numerical simulation is preformed using CFD software tool Fluent 6.1. Electrochemical model is programmed in C compile language. It is solved coupling with Navier–Stokes equation through the UDF interface tool that is provided in Fluent 6.1. To validate the model, a single tubular and a planar geometries SOFC were simulated using the same as present numerical model and program in references [12,23]. The simulation results were good agreement with the experiment data and benchmark data, respectively. In present simulation case, the mean current density is 2793 A/m^2 and it has 4.6% error comparing to the experimental data 2670 A/m^2 given by Siemens–Westinghouse Corporation in reference [3].

For discussion, two areas called the middle zone and the corner zone are defined in this study (see Fig. 6). Fig. 6 shows the distribution of gaseous molar fraction in the fuel channel. The reactant gas species H_2 decreases along the flow direction due

Table 1
Material properties and operating conditions [1,3,4,22]

	Cathode	Electrolyte	Anode	Inter-connector
σ	$1.232 \times 10^4 e^{-600/T}$	$3.401 \times 10^4 e^{-10350/T}$	$1.117 \times 10^7 e^{1392/T}$	$3.981 \times 10^3 e^{-4690/T}$
λ	6.23	2.7	9.6	10.0
Operating conditions				
Operating pressure (bar)			2.9	
Operating voltage (V)			0.610	
Electrode porosity			0.3	
Fuel utilization			85%	
Air intake rate (kg/s)			7.55e − 04	
Gas inlet temperature (K)			1123 K for fuel inlet, 1073 K for air inlet	
Inlet gas composition		Air: O_2 21%, N_2 79% Fuel: H_2 21.7%, H_2O 31.7%, CO 5.7%, CO_2 22.3%, CH_4 12.3%, N_2 6.3%		
The exchange current parameters [22]		$\gamma_a = 5.5 \times 10^8$ A/m^2, $E_a = 1.0 \times 10^5$ J/mol		
		$\gamma_c = 7.0 \times 10^8$ A/m^2, $E_c = 1.2 \times 10^5$ J/mol		

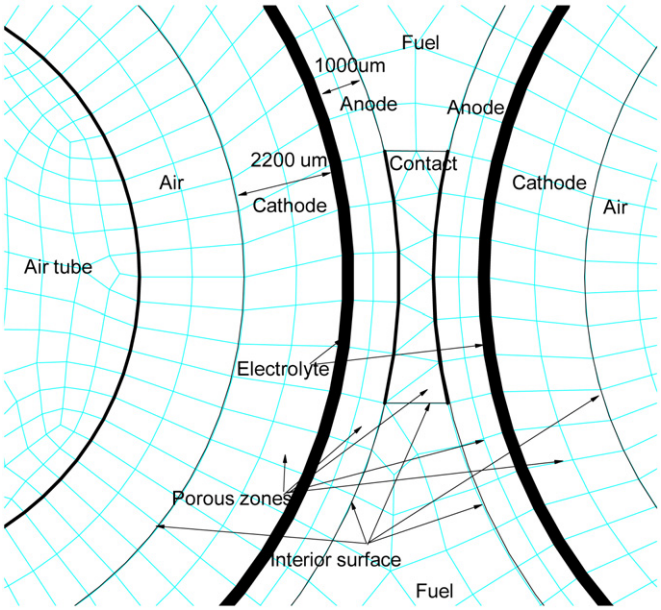

Fig. 5. The topology of the grid around the electrolyte.

to the electrochemical reaction, while the product of the electrochemical reaction H_2O increases as the gases flow toward the outlet. Accordingly, the water-gas shift reaction presents more positive trend while the molar fraction of H_2O increases and H_2 molar fraction decreases along the stream at fuel side. Therefore, the CO molar fraction decreases but the CO_2 molar fraction rises from the inlet to the outlet at the anode side. As can be seen in Fig. 6, lower molar fraction of H_2 and CO with higher molar fraction of H_2O and CO_2 were formed in the middle zone between each of unit-cell comparing to that of the corner zone, which could be interpreted with two reasons. One is that the spatial volume within the middle zone is smaller than that of corner zone and the space affects the velocity of gases species diffusion (as the velocity vector shown in Fig. 8). Another reason is that there is an open circumference (see Fig. 3) at the anode and the electrolyte around corner zone, which causes the chemical reactive area to be smaller than that of middle zone. Therefore, it is very easy to generate local fuel starvation in the middle active zone if the fuel utilization is too high. Even in the case of normal fuel utilization, fuel starvation might occur within the middle active zone. There exists an optimum space between cells that acquires the SOFC peak efficiency with definite fuel utilization.

The heat was produced ascribed to the chemical reaction and the electric resistance. The electrochemical reaction and the positive direction of shift reaction are exothermal while the fuel reforming is endothermic. Table 2 summarizes the generated total heat on the whole simulation field according to the simulation results. The data is calculated with the integral method in the whole computation field. The total generated heat is 220 W without including the absorption heat by the reforming process. 91% of the total generated heat is attributed to the chemical reactions within fuel cell. The ohmic heat contributes 9% in the total generated heat due to electric resistance within the electric components. As we know, the methane reformation is endothermic reaction. If the total generated heat is subtracted by the reforming process within the indirect internal reformer, then the percentage of ohmic heat in the total released heat is up to 17.3%. This value is higher than that of 8% for the same geometries tubular SOFC without internal reformer, which was presented in reference [12]. The maximum part in the total ohmic heat is come from the cathode, which contributes 79.6%. This is caused due to the design and configuration of tubular SOFC. One hand, the route of current within cathode is much longer than that of both electrolyte and inconnector. On the other hand, the electric conductivity of cathode is much lower than that of anode. The second part after the cathode is the inter-connector with 16.4% contribution to the total ohmic heat. According to the data in Table 2, we can calculate the percentage of the absorption heat associated with the reforming process, air flow and fuel flow in the total generated heat. 47.3% of the sum of the generated heat within the cell is absorbed by the endothermic process of fuel reforming in the reformer. Furthermore, calculation results show that about 36.6% of the generated heat is taken out by the air, which is greater than 16% of the heat taken out by the fuel stream.

The temperature distribution is shown in Fig. 7. The temperature increases along the fuel stream since the electrochemical reaction is exothermic process. At the downstream of the fuel, the temperature decreases with the fuel stream flow to the outlet, which is due to the coolant effect by the incoming inlet air in the air feed tube. The minimum temperature is found

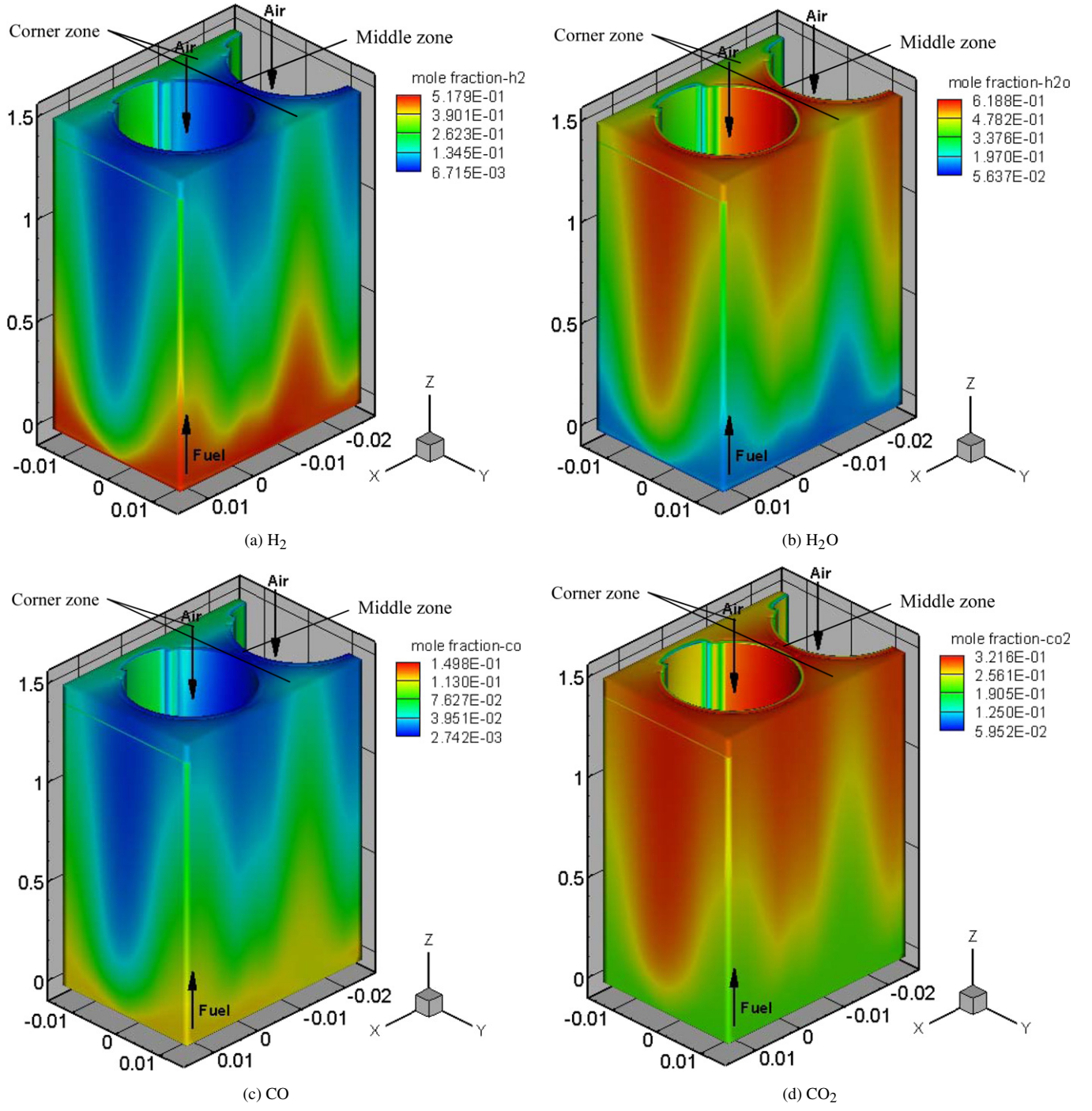

Fig. 6. Distribution of gas species molar fraction in the fuel channel.

Table 2
Summary of the generated heat

	Fueled with indirect internal reformer					Fueled with hydrogen [12]
	Anode	Cathode	Electrolyte	Inter-connector	Reformer	
$Q_{chem}(W)$	200.0	0	0	0	−104.0	78.1
$Q_{ohm}(W)$	0.2	16.0	0.6	3.3	0	6.8
$Q_{ohm}/Q_{ohm,tot}$ (%)	1.0	79.6	3.0	16.4	–	–
Q_{ohm}/Q_{tot} (%)			17.3			8.0

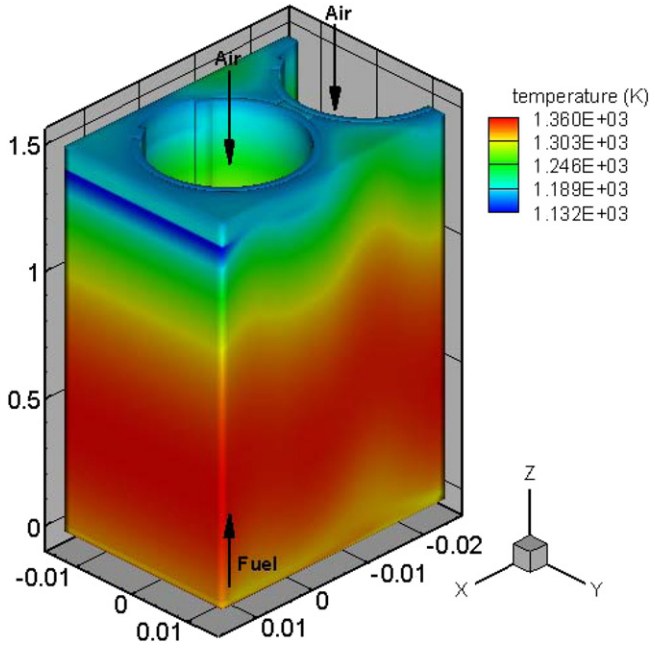

Fig. 7. Distribution of the temperature in the fuel channel.

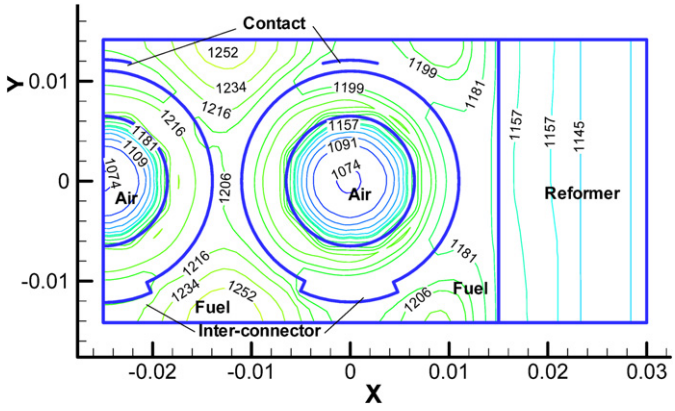

(a) Contour of temperature (K, $z = 1.35$ m)

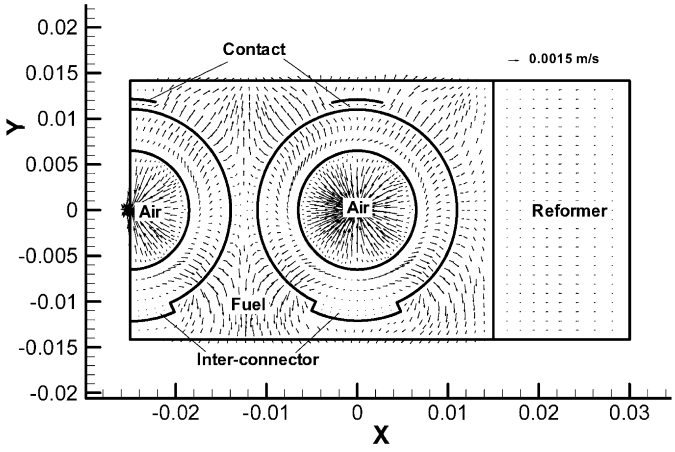

(b) Vector of velocity ($z = L/2$)

Fig. 8. The velocity vector and the distribution of temperature.

at the location nearest to the reformer where the endothermic reformation of methane absorbs much of the thermal energy produced by the cell.

Fig. 8(a) shows the temperature distribution in the profile $z = 1.35$ m. The heat of electrochemical reaction is produced around the electrolyte. These heats are shifted to the gas mainstreams for both of fuel and air by the way of thermal convection and conduction. As shown in Fig. 8(a), air is pre-heated in the bleed tube before it enters cathode side. At the fuel side, the gradient of temperature is relatively smaller comparing to that of air side. A higher temperature area occurs at the corner zone. On the one hand, the higher temperature gases around the electrochemical reaction site are transferred to the fuel channel with gases diffusion. On the other hand, the negative direction of gas-water shift reaction is exothermic. Therefore, there is higher hydrogen molar fraction and lower water molar fraction at the corner zone comparing to the middle zone according to Fig. 6. This tendency makes the gas-water shift reaction present more negative direction. Fig. 8(b) shows the vector of gaseous velocity in the middle profile. The gases species in the air channel flow to the cathode catalyze interlayer, where the oxygen is consumed beside the electrolyte for the reason of the electrochemical reaction. Accordingly the water is produced in the anode side field and the gases species diffuse from the anode catalyze interlayer to the fuel channel.

Fig. 9 shows the contour of current density and the heat produced due to the ohmic resistance at the middle profile $z = L/2$. As shown in Fig. 9(a), the current density in the anode decreases with the current flow because the current passes through the electrolyte from the anode to the cathode. Therefore, the current density increases along the current flow at the cathode side. Furthermore, since the anode thickness is much less than that of cathode, the current density in the anode is much higher than that in the cathode. Fig. 9(b) shows the distribution of the produced heat caused by electric resistance. Much of the ohmic heat comes from the cathode side ascribed to the large electric resistance. The maximum ohmic heat occurs at the contact of the cathode and the inter-connector. It is also more possible that the excess threshold of thermal gradient arises from this area. At the anode side, the ohmic heat can be almost neglected even though the current density is very high.

5. Conclusions

A three-dimensional numerical model of SOFC is developed based on the complete polarization mathematic mode in the present study. Numerical simulation is implemented on a tubular solid oxide fuel cell stack with indirect internal fuel reformer. The mean current density acquired by the numerical simulation is agreement with the experiment data for the SOFC stack. The thermal characteristics of the SOFC stack are investigated based on the simulation results.

Numerical simulation shows that the molar fractions of the gaseous species perform very non-uniform in the normal section of the gas flow direction. The reactant concentration within the middle zone is much lower than that of the corner zone due to the spatial effect. Fuel depleted regions might first appear in the middle zone if the provided fuel decreases or the fuel uti-

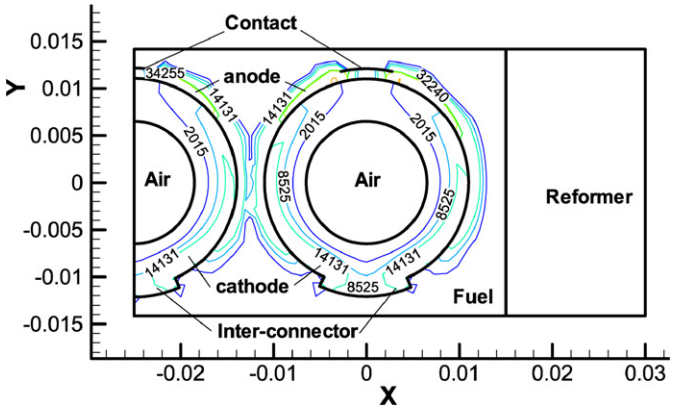

(a) The contour of current density (A/m^2)

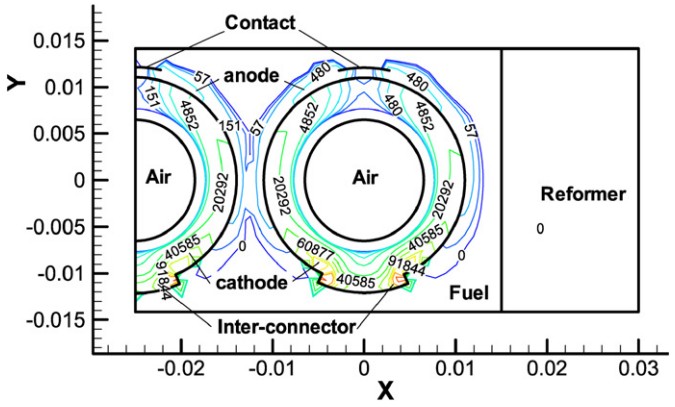

(b) The ohmic heat distribution (W/m^3)

Fig. 9. Distribution of electric characteristic in the middle profile ($z = L/2$).

lization increases. In order to avoid the fuel starvation to be happen, the space between each of the cells should be made as large as possible in the design of SOFC stack. In the generated total heat within the cell, the heat generated by the chemical reactions contributes to 91% and the ohmic generated heat contributes to 9%. Since the ohmic heat is produced in very small volume components such as inter-connector, the cathode and the electrolyte, it might makes the component exceed the temperature limit or the temperature grads limit. Simulation results also show that as much as 79.6% of the ohmic heat comes from the cathode. The second contributor is inter-connector, which possesses about 16.4 % in the total ohmic heat. The high ohmic heat is found around the contact between the inter-connector and the cathode. As much as 47.3% of the generated total heat is absorbed by the reforming reaction. The air flow and the fuel flow take away 36.6% and 16%, respectively. In the fuel flow direction, the highest temperature area is found in the middle of stack.

Acknowledgement

The research work was supported by the Doctor Foundation of Xi'an Jiaotong University (No. DFXJTU2005-01).

References

[1] Fuel Cell Handbook, sixth ed., EG & G Technical Services, Inc. Science Applications International Corporation, U.S. Department of Energy Office of Fossil Energy, National Energy Technology Laboratory, West Virginia, 2002.
[2] A.D. Rao, A thermodynamic analysis of tubular SOFC based hybrid systems, Ph.D. Thesis, University of California, Irvine, USA, 2001.
[3] S.E. Veyo, L.A. Shockling, J.T. Dederer, J.E. Gillett, W.L. Lundberg, Tubular solid oxide fuel cell/gas turbine hybrid cycle power system: status, ASME J. Engineering for Gas Turbines and Power 124 (2002) 845–849.
[4] N.F. Bessette II, W.J. Wepfer, J. Winnick, A mathematical model of a solid oxide fuel cell, J. Electrochem. Soc. 142 (1995) 3792–3800.
[5] C.L. Haynes, Simulation of tubular solid oxide fuel cell behavior for integration into gas turbine cycles, Ph.D. Thesis, Georgia institute of technology, USA, 1999.
[6] J.R. Ferguson, J.M. Fiard, R. Herbin J, Three-dimensional numerical simulation for various geometries of solid oxide fuel cells, J. Power Sources 58 (1996) 106–122.
[7] P.-W. Li, K. Suzuki, Numerical modeling and performance study of a tubular SOFC, J. Electrochem. Soc. 151 (2004) 548–557.
[8] R.J. Braun, Optimal design and operation of solid oxide fuel cell systems for small-scale stationary applications, Ph.D. Thesis, University of Wisconsin–Madison, USA, 2002.
[9] N. Autissier, D. Larrain, J.V. Herle, D. Favrat, CFD simulation tool for solid oxide fuel cells, J. Power Sources 131 (2004) 313–319.
[10] S. Campanari, P. Iora, Definition and sensitivity analysis of a finite volume SOFC model for a tubular cell geometry, J. Power Sources 132 (2004) 113–126.
[11] M.A. Khaleel, Z. Lin, P. Singh, W. Surdoval, D. Collin, A finite element analysis modeling tool for solid oxide fuel cell development: coupled electrochemistry, thermal and flow analysis in MARC, J. Power Sources 130 (2004) 136–148.
[12] X. Zhang, G. Li, J. Li, Z. Feng, Numerical study on the electric characteristics of solid oxide fuel cells, Energy Conversion and Management 48 (2007) 977–989.
[13] S.H. Chan, K.A. Khor, Z.T. Xia, A complete polarization model of a solid oxide fuel cell and its sensitivity to the change of cell component thickness, J. Power Sources 93 (2001) 130–140.
[14] J.T. Brown, Solid oxide fuel cell technology, IEEE Transactions on Energy Conversion 1988 (2) (1988) 193–198.
[15] Siemens celebrates on-year anniversary of SOFC generator in Italy, Fuel Cells Bulletin, September 2006, p. 3.
[16] M. Cali, M.G.L. Santarelli, P. Leone, Computer experimental analysis of the CHP performance of a 100 kWe SOFC field unit by a factorial design, J. Power Sources 156 (2006) 400–423.
[17] Raymond A. Georgr, Status of tubular SOFC field unit demonstrations, J. Power Sources 86 (2000) 134–139.
[18] E. Achenbach, E. Riensche, Methane-stream reforming kinetics for solid oxide fuel cells, J. Power Sources 52 (1994) 283–288.
[19] H. Yakabe, T. Ogiwara, M. Hishinuma, I. Yasuda, 3-D model calculation for planar SOFC, J. Power Sources 102 (2001) 144–154.
[20] W.Q. Tao, Numerical Heat Transfer, second ed., Xi'an Jiaotong University Press, Chinese, 2001.
[21] Fluent User's Guide, Version 6.1. Fluent Inc., Lebanon, NH, 2003.
[22] P. Costomagna, A. Selimovic, M.D. Borghi, G. Agnew, Electrochemical model of the integrated planar solid oxide furl cell (IP-SOFC), Chem. Eng. J. 102 (2004) 61–69.
[23] X. Zhang, J. Li, G. Li, Z. Feng, Development of a control-oriented dynamic model for the solid oxide fuel cell, J. Power Sources 160 (2006) 258–267.